

Modeling betatron radiation using particle-in-cell codes for plasma wakefield accelerator diagnostics

M. Yadav^{1,2,3,*}, C. Hansel⁴, B. Naranjo¹, G. Andonian¹, P.

Manwani¹, Ö. Apsimon⁵, C.P. Welsch^{2,3}, and J. B. Rosenzweig¹

¹*Department of Physics and Astronomy, University of California Los Angeles, California 90095, USA*

²*Department of Physics, University of Liverpool, Liverpool L69 3BX, UK*

³*Cockcroft Institute, Warrington WA4 4AD, UK*

⁴*Center for Integrated Plasma Studies, Department of Physics, University of Colorado Boulder, Boulder, Colorado 80309, USA and*

⁵*Department of Physics and Astronomy, University of Manchester, Manchester M19 3PL, UK*

(Dated: March 9, 2023)

The characterization of plasma wakefield acceleration experiments using emitted photons from betatron radiation requires numerical models in support of instrumentation of single-shot, double-differential angular-energy spectra. Precision characterization for relevant experiments necessitates covering a wide energy range extending from tens of keV through 10 GeV, with an angular resolution on the order of 100 μrad . In this paper, we present a numerical model for betatron radiation from plasma accelerated beams, that are based on integration of LinardWiechert (LW) potentials for computed particle trajectories. The particle trajectories are generated in three different ways: first, by particle tracking through idealized fields in the blowout regime of PWFA; second, by obtaining trajectories from the Quasi-static Particle-in-Cell (PIC) code `QuickPIC`; and third, by obtaining trajectories from the full PIC code `OSIRIS`. We performed various benchmarks with analytical expressions and the PIC code `EPOCH`, which uses a Monte-Carlo QED radiation model. Finally, we present simulations of the expected betatron radiation for parameters from the Facility for Advanced Accelerator Experimental Tests II (FACET-II) PWFA and plasma photocathode experiments.

I. INTRODUCTION

Beam driven plasma wakefield accelerators (PWFAs) have already demonstrated [1] acceleration gradients orders of magnitude higher than the limits of conventional radio-frequency acceleration and are envisioned as the core technology for next-generation, compact high-energy particle accelerators. In PWFA, a drive electron beam in a plasma excites a wakefield that accelerates a trailing (witness) electron beam. The Facility for Advanced Accelerator Experimental Tests (FACET) at SLAC National Accelerator Laboratory [2], the predecessor facility to FACET-II, achieved several key milestones toward realizing practical PWFAs including high-efficiency acceleration [3], high total energy gain [4], positron acceleration [5], and the demonstration of a plasma photocathode [6], also known as Trojan horse. The FACET-II facility [7, 8] aims to build on these accomplishments by demonstrating high beam quality of accelerated and plasma-injected beams and testing several new concepts for acceleration, manipulation, and radiation generation. However, measuring many key results of these experiments is a significant challenge for conventional diagnostics, due to the extremely low emittances, potentially large correlated energy spread, and jitter of the anticipated beams. While using advanced machine learning (ML) methods [9–11] are viable for predicting the longitudinal phase-space, non-destructive inference of transverse beam emittance, and spectral reconstruction

of the bunch profile, electron beam facilities will also rely on betatron radiation as a critical mechanism to augment the diagnostic capacity.

In a PWFA, betatron radiation [12–14] is produced due to the transverse betatron oscillations of charged particles. Betatron radiation is beneficial not only as a radiation source, but also as a carrier of detailed information about beam-plasma interaction. Employing betatron radiation as a diagnostic has the advantage of being both single-shot and non-destructive to the beam. The betatron radiation signal is accessible due to the large radiation flux generated by relativistic beams in plasmas. Betatron radiation diagnostics have been utilized in inverse Compton scattering experiments [15], and studied in proton-driven PWFA experiments at AWAKE [16, 17]. While the implementation of betatron radiation diagnostics was attempted at FACET, the high emittance of the beams prevented it from meeting its full potential. The betatron diagnostic system will provide both angular and spectral information about the emitted betatron radiation on a shot-by-shot basis, yielding critical information about the plasma accelerated beam.

In order to practically infer information about the beam from betatron radiation, fast and accurate numerical models are required. Betatron radiation models should generate large datasets for ML, or used within a maximum likelihood estimation algorithm (MLE), or similar. Recent work [18–22] has utilized data from simulated PWFA betatron radiation experiments to reconstruct beam parameters using ML methods reliably. However, the radiation spectrum in this preliminary analysis extends beyond 100 MeV due to the very high plasma

* monika.yadav@liverpool.ac.uk

density and concomitant focusing strength. Studies of the changes to this spectrum due to instabilities and more significant amplitude betatron motion are now underway.

This work discusses novel radiation algorithms to study the radiations emitted by beam plasma interactions. There are various techniques to compute the motion of charged particles, including analytical methods mathematically modeling the charged particle's motion using equations of motion and solving them analytically. Numerical integration using Runge-Kutta method, computational approach to model charged particle dynamics in plasma by treating particles as discrete entities and solving equations of motion in a self-consistent manner. A statistical Monte Carlo simulation technique for simulating the motion of charged particles by randomly sampling their path through space and averaging the results over many runs. In this paper, we introduce numerical models for computing betatron radiation spectrum from PWFAs and plasma injectors that can be used to reconstruct beam parameters from betatron radiation signatures. Radiation is computed based on integration of LW potentials for computed particle trajectories using different PIC codes. The radiation spectra for different models are validated, compared, and used to simulate expected radiation properties from planned PWFA and plasma injector experiments at FACET-II. Spatial and temporal profiles of radiation are also important to study orbital angular momentum of light, microscopy of lights [23].

In Sec. II, we lay out a limited analytical description of the betatron radiation generated by a Gaussian beam in an ion channel. In Sec. III, we discuss numerical models for betatron radiation from plasma accelerated beams for computed particle trajectories for different PIC code. In Secs. IV and V, we present simulations of planned PWFA and plasma injection experiments, respectively, and discuss generally expected features of the radiation. Finally, in Sec. VI, we conclude with numerical modeling of betatron radiation and betatron radiation diagnostics in general.

II. ANALYTIC DESCRIPTION OF THE RADIATION SPECTRUM

In this section, we present an analytic model of betatron radiation in PWFA, beginning with the single-particle spectrum derivation and extending it to a particle distribution. In the blowout regime [24], the drive beam leaves behind an ion channel that can be assumed uniform provided ion motion [25] is insignificant. For paraxial ($\mathbf{p}_\perp \ll p_z$) motion, beam electrons undergo simple harmonic motion with a betatron angular wavenumber, $k_\beta = k_p/\sqrt{2\gamma}$, where γ is the Lorentz factor, $k_p = \sqrt{4\pi r_e n_0}$ is the plasma angular wavenumber, n_0 is the plasma density, and r_e is the classical electron radius [14]. Beam electrons produce undulator radiation with an equivalent strength parameter $K = \gamma k_\beta r_\beta$, where r_β is the particle's maximum oscillation amplitude.

In the ion channel, each particle of an on-axis beam has a different value of K , due to different oscillation amplitudes. Contrasted with undulator radiation, where K is constant, the spectra of PWFA betatron radiation crosses different regimes. There are three regimes of undulator radiation [13]. For $K \ll 1$, radiation is emitted in a cone containing angles $\theta \lesssim 1/\gamma$, where θ is the radiation cone opening angle. Then, the radiation spectrum is sharply spiked around the total photon energy $\epsilon_1 = 2\hbar c\gamma^2 k_\beta/(1 + \gamma^2\theta^2 + K^2/2)$. Then, for $K \sim 1$, integer harmonics of the fundamental begin to be generated, and the radiation is emitted in the broader cone containing angles $\theta \lesssim K/\gamma$. More harmonics are produced for larger K . Finally, for $K \gg 1$, the harmonics blend to form a smooth synchrotron radiation spectrum characterized by a critical photon energy $\epsilon_c = 3\hbar c K\gamma^2 k_\beta/2$.

These three regimes describe the spectra produced by a single particle. The total radiation is given by the integral over a range of K for a beam. Provided the beam spot size $\sigma_r \gg 1/(\gamma k_\beta)$, many of the particles in the beam are in the $K \gg 1$ regime, and since those particles generate significantly greater number of photons than a particle with small K , the overall radiation emitted by the beam is dominated by them.

The radiation of a single particle in the $K \gg 1$ regime is, assuming no \hat{z} angular momentum,

$$\left(\frac{dI}{d\epsilon}\right)_{sp} = \frac{I_{\text{tot},sp}}{\epsilon_{c,sp}} S_{sp} \left(\frac{\epsilon}{\epsilon_{c,sp}}\right) \quad (1)$$

where $\epsilon_{c,sp}$ and $I_{\text{tot},sp}$ are the critical photon energy and total radiated energy by a single particle, respectively which is given by [12]

$$I_{\text{tot},sp} = \frac{1}{6} r_e m_e c^2 k_p^4 L_p \gamma^2 r_\beta^2, \quad (2)$$

$$\epsilon_{c,sp} = \frac{3}{4} \hbar c k_p^2 \gamma^2 r_\beta, \quad (3)$$

and

$$S_{sp}(x) = \frac{9\sqrt{3}}{8\pi} x \int_x^\infty K_{5/3}(y) dy \quad (4)$$

where K is the Bessel function. $S_{sp}(x)$ is the universal function of synchrotron radiation [13], which satisfies the normalization condition $\int_0^\infty S_{sp}(x) dx = 1$. The single particle spectrum can be integrated over the beam distribution to express the spectrum of the total radiation produced by the beam. For a monochromatic Gaussian beam, the spectrum is

$$\begin{aligned} \left(\frac{dI}{d\epsilon}\right)_b &= 2\pi \int_0^\infty \left(\frac{dI}{d\epsilon}\right)_{sp} \frac{Q}{2\pi\sigma_\perp^2} e^{-\frac{r_\beta^2}{2\sigma_\perp^2}} r_\beta dr_\beta \\ &= \frac{I_{\text{tot},b}}{\epsilon_{c,b}} S_b \left(\frac{\epsilon}{\epsilon_{c,b}}\right) \end{aligned} \quad (5)$$

where Q is the total beam charge, and σ_{\perp} is the average radius of the beam particles,

$$S_b(x) = \frac{9\sqrt{3}\Lambda^4}{16\pi} x^3 \int_0^{\infty} \int_v^{\infty} \frac{K_{5/3}(u) e^{-\frac{\Lambda^2 x^2}{2v^2}}}{v^3} dudv, \quad (6)$$

$$I_{\text{tot},b} = \frac{1}{3e} r_e m_e c^2 k_p^4 L_p Q \gamma^2 \sigma_r^2, \quad (7)$$

and

$$\epsilon_{c,b} = \frac{3}{4} \Lambda \hbar c k_p^2 \gamma^2 \sigma_r \quad (8)$$

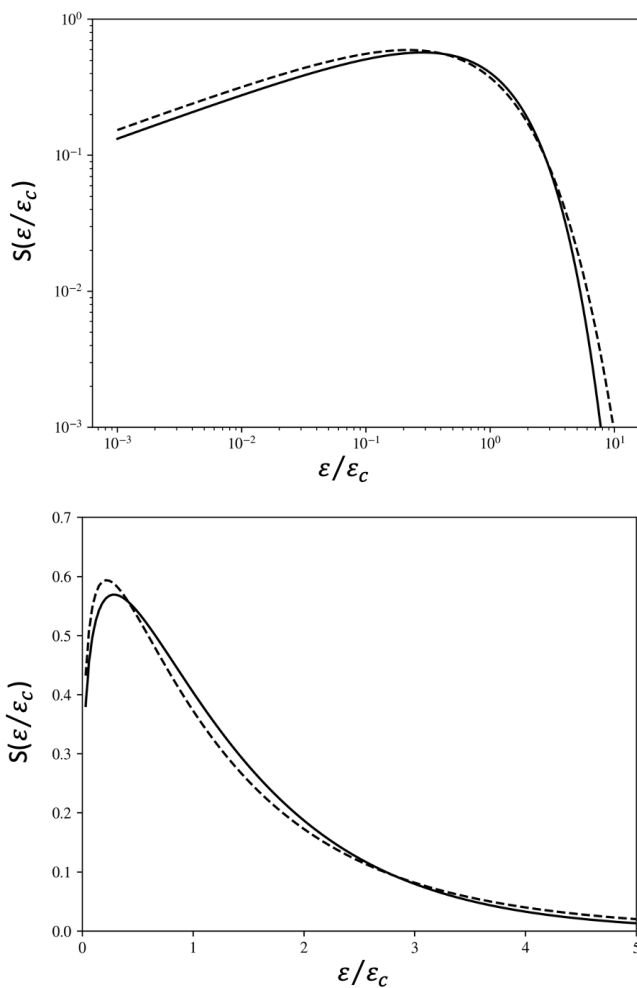


FIG. 1: Normalized analytic betatron radiation spectra as functions of the normalized radiation energy. Solid line: Single particle spectrum $S_{sp}(\epsilon/\epsilon_c)$ given by equation (4). Dashed line: Beam spectrum $S_b(\epsilon/\epsilon_{c,b})$ given by Eq. (6).

where Λ is a dimensionless constant determined using the precise definition of the critical energy. We have defined

$S_b(x)$ such that it satisfies the same normalization condition as $S_{sp}(x)$: $\int_0^{\infty} S_b(x) dx = 1$. The critical energy ϵ_c is defined as the energy for which [26]

$$\int_0^{\epsilon_c} \frac{dI}{d\epsilon} d\epsilon = \int_{\epsilon_c}^{\infty} \frac{dI}{d\epsilon} d\epsilon. \quad (9)$$

In order to define $\epsilon_{c,b}$ such that this is satisfied in the beam case, the constant Λ must satisfy

$$\int_0^{\infty} \left[1 - e^{-\frac{\Lambda^2}{2x^2}} \left(1 + \frac{\Lambda^2}{2x^2} \right) \right] S(x) dx = \frac{1}{2}. \quad (10)$$

Numerically evaluating this gives $\Lambda \approx 1.7231$. A plot of $S_{sp}(x)$ and $S_b(x)$ is shown in Fig. 1. From this plot, it is clear that the overall shape of the normalized single particle and beam spectra $S_{sp}(x)$ and $S_b(x)$ are similar. Overall while these equations are of some usefulness, they do not account for many of the important effects that may influence betatron radiation, such as acceleration, energy spread, \hat{z} angular momentum of beam electrons, plasma ramps, and the contribution of the low K core of the beam.

III. NUMERICAL MODELS OF BETATRON RADIATION

This section presents three numerical models for computing betatron radiation at three increasing fidelity, and computational cost, levels. Higher grid resolution is required to capture short wavelength radiation using PIC algorithms, leading to high computational expensive codes.

A. Idealized particle tracker with LinardWiechert radiation

We developed a betatron radiation code that tracks particles through idealized fields and computes the emission of electromagnetic radiation by charged particles undergoing betatron oscillations using LinardWiechert (LW) potentials. The code is written in C++ and parallelized using Boost.MPI allowing for large simulations. First, macro-particles are randomly sampled from a Gaussian beam distribution. Next, particles are tracked through idealized acceleration and focusing fields using a 4th-order Runge-Kutta (RK4) integration method. The fields used are a linear focusing force from the ion channel and a constant accelerating field $\mathbf{E} = Z_i m_e \omega_p^2 \mathbf{r}_{\perp} / 2e + E_{\text{accel}} \hat{z}$ where E_{accel} is an input parameter. The electron trajectories are used to integrate the complex LW potential for particle i numerically.

$$\mathbf{V}_i = \int_{t_i}^{t_f} \frac{\mathbf{n} \times ((\mathbf{n} - \boldsymbol{\beta}) \times \dot{\boldsymbol{\beta}})}{(1 - \mathbf{n} \cdot \boldsymbol{\beta})^2} e^{\frac{i\epsilon}{\hbar}(t - \mathbf{n} \cdot \mathbf{r}(t)/c)} dt \quad (11)$$

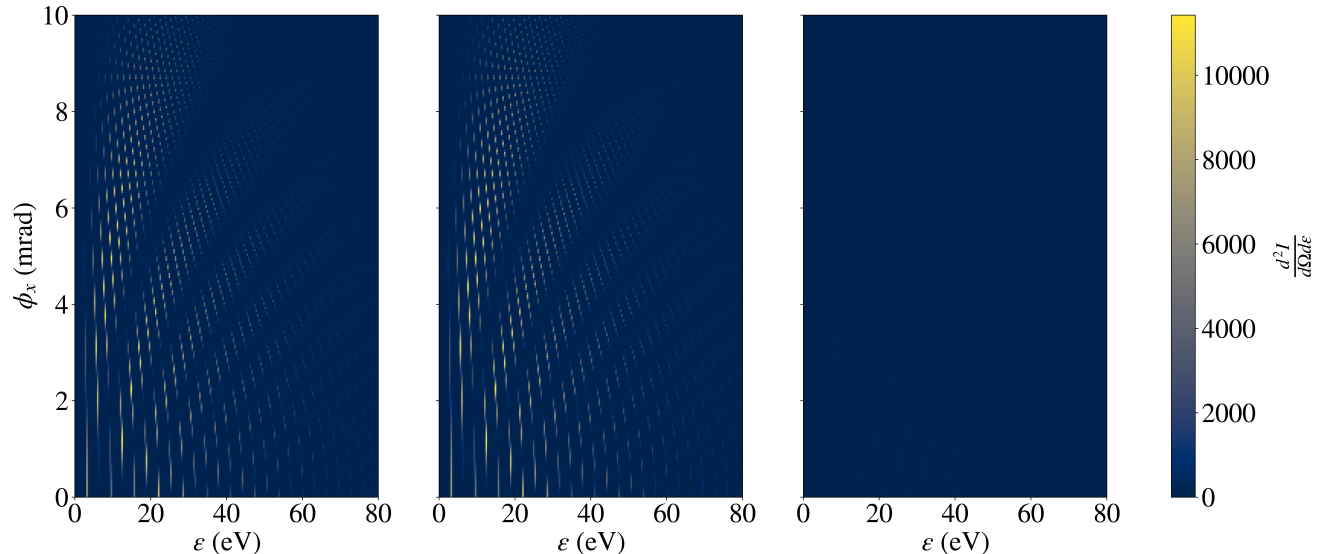


FIG. 2: Double differential spectra for the second benchmark of the model III A. Left: Analytical spectrum. Middle: Spectrum computed by a model III A. Right: Absolute error between the two spectra.

Table I: Parameters for the second benchmark simulation for the idealized particle tracker and LW.

Parameter	Value	Unit
Plasma density	4×10^{16}	cm^{-3}
Plasma length	60	cm
Beam energy	10	GeV
Beam charge	500	pC
Beam spot size	4.5	μm
Beam normalized emittance	0 or 75 ^a	mm-mrad
Simulation particles	500	
Step size	12	μm
$\phi_{x,y}$ window	$[-1.5, 1.5]$	mrad
$\phi_{x,y}$ points	51	
ϵ range	$[0.5, 5000]$	keV
ϵ points	101	
ϵ spacing	logarithmic	

^a Two simulations were performed, one with zero emittance and one with matched emittance.

where \mathbf{n} is the average vector in the direction of the radiation observation direction, β is the velocity of the electron normalized to the speed of light c , β is the usual acceleration divided by speed of light and ϵ is the photon energy. \mathbf{V}_i is computed over a 3D grid of different directions and photon energies. This computation takes place simultaneously with particle tracking, the particle data does not have to be saved and can be discarded after it has been used to compute the fields. Each Message Passing Interface (MPI) process computed its contribution to the radiation independently and in parallel and summed at the end. The double differential spectrum is given by

$$\frac{d^2 I}{d\Omega d\epsilon} = \frac{e^2}{16\pi^3 \epsilon_0 \hbar c} \left| \sum_i w_i \mathbf{V}_i \right|^2 \quad (12)$$

where $w_i \equiv \sqrt{|Q_{i,\text{macroparticle}}|/e}$ is the particle weight. The primary bottleneck is the $O(N^3)$ scaling of the 3D grid resolution and the small time step required to prevent aliasing, particularly at high ϵ . While the number of simulated particles is typically small, even with just a few hundred, the statistical error in computed radiation tends to be low.

We performed two tests to benchmark the code. We tracked a single particle through an ion channel in the first test. The particle had an energy $E = 100$ MeV, undulator parameter $K = 2$, and betatron period $\lambda_\beta = 1$ cm. It was tracked for 10 periods with 100 steps per period. The analytical and numerical double differential spectra and the absolute error between them are shown in Fig. 2, demonstrating agreement between simulation and theory. For the second benchmark, we tracked a beam with parameters roughly based on PWFAs experimental plans at FACET-II, which are shown in Table I. Two simulations were performed, one with zero emittance and one with finite emittance, such that the spot size was matched to the plasma $\epsilon = \gamma k_\beta \sigma_r^2$. The spectra from both of these simulations are shown compared to the analytic expression from Eq. (5) in Fig. 3.

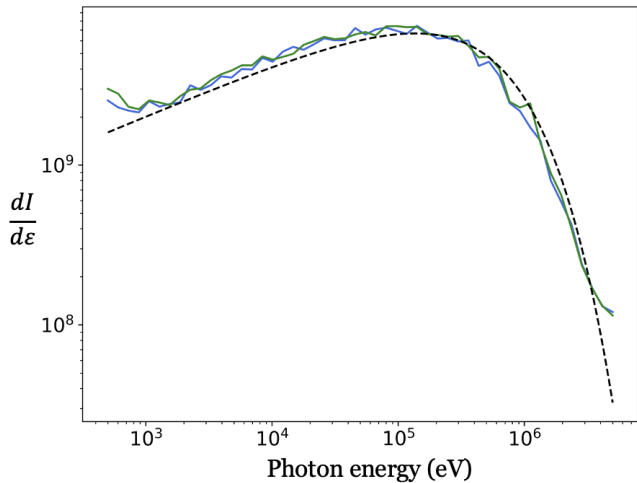


FIG. 3: Synchrotron radiation spectra for the second benchmark of the model III A. Blue: simulation with zero emittance. Green: simulation with matched emittance. Black, dashed: analytic spectrum.

B. Quasi-Static Particle-in-Cell with Linard Wiechert Radiation

At the next level of sophistication, we computed betatron radiation from the 3D Quasi-static PIC code QuickPIC [27, 28]. Quasi-static PIC codes use the approximation that the beam evolves on a much slower timescale than the plasma wake to achieve significant speedups over conventional PIC codes. This approximation is accurate when simulating PWFA but prevents Quasi-static from simulating plasma injectors or non-relativistic beams. Compared to that of Sec. III A, this numerical model can accurately describe the radiation from the drive beam, which is only partially inside the ion channel, and it can accurately describe the radiation signature of effects such as hosing. While QuickPIC does not directly compute radiation, we modified it to output particle trajectories and input a randomly selected subset of those into a code based on the LW code discussed in Sec. III A. This approach is similar to the method used in [29] to compute betatron radiation.

When computing the LW potential integral Eq. (11), the step size required to accurately compute high energy radiation without aliasing effects is very small, typically much smaller than the step size required to track particles accurately. In order to compute this high energy radiation, additional trajectory points were interpolated between the points computed by QuickPIC using cubic B-spline interpolation. This was not done in Sec. III A because the speed of the simple RK4 tracker in Sec. III A meant that particles could be tracked with smaller steps than needed while barely increasing computation time. Additionally, the LW code used in this section used Python’s `multiprocessing` module, and computed radiation after particle tracking finished.

Table II: Parameters for III B benchmark simulation

Parameter	Value (Drive, Witness)	Unit
Plasma density	4×10^{16}	cm^{-3}
Plasma length	60	cm
Plasma radius	31.9	μm
Beam energy	10, 10	GeV
Beam charge	500, 500	pC
Beam spot size	5, 4.5	μm
Beam length	5, 2.8	μm
Beam norm. emit.	3.2, 3	mm-mrad
Beam separation	101.55	μm
QuickPIC Resolution	$1.04 \times 1.04 \times 0.60$	μm
QuickPIC Time step	1.10	ps
QuickPIC Macro-particles	64^3	
LW particles	100	
LW time step	66.7	fs
LW angular window	$[-1, 1]$	mrad
LW angular grid points	25×25	
LW angular grid spacing	linear	
LW energy window	$[5 \times 10^3, 5 \times 10^6]$	eV
LW energy grid points	50	
LW energy grid spacing	logarithmic	

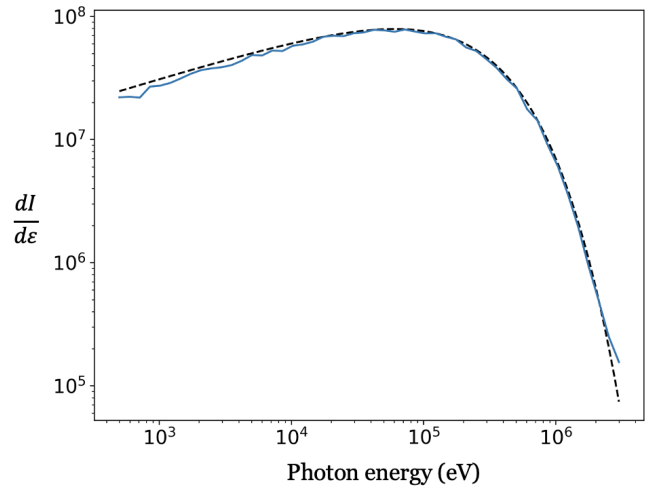


FIG. 4: Blue: Radiation spectrum computed numerically using the III B. Black, dashed: Analytical radiation spectrum given by Eq. (5).

In order to benchmark this code against Eq.(5), we used parameter set, shown in Table II, that minimized witness beam acceleration by placing it at the longitudinal wakefield’s zero crossing. Only the radiation from the witness beam was computed, and the time evolution of the drive beam was turned off. The computed spectrum, shown in Fig. 4, agrees with the theoretical spectrum.

C. Full Particle-in-Cell OSIRIS code with LinardWiechert Radiation

We will use the OSIRIS code to simulate the FACET-II Trojan horse experimental scenario. These simulations focuses on generating the witness beam using plasma photocathodes and collinear laser ionization injection scheme. In the end, we will focus on calculating betatron radiation importing trajectories obtained from OSIRIS to Sec. III A. A plasma profile comprising a vacuum section followed by an increasing short ramp section was implemented. The zero density section is provided for the initialization of a laser pulse by ensuring the consistency of Maxwell's equations. A laser pulse is used in OSIRIS code defining 3D Gaussian beam profiles. Leading order corrections on the longitudinal electric field for the diffraction angle expansion and short pulse duration are implemented. The model featured control on parameters for focal spot position and temporal pulse center and longitudinal magnetic fields for out-of-plane laser polarization. An 800 nm laser with a spot size of few μm was initiated at the zero density region with a normalized vector potential value of $a_0 = 0.02$. The spot size is chosen to provide suitably large field regions for the injection of the probe beam. A matched plasma channel width of 250 μm was defined for a plasma density of $1.79 \times 10^{22} \text{ m}^{-3}$ to ensure a constant laser spot size during the propagation and a 30 cm long dephasing length that is equal to the foreseen plasma length for future experimental studies. Experimentally, a cryogenically-cooled gas jet operated at many atmospheres of pressure may be used to produce the required density [30]. The laser used to ionize the HIT gas is within the blowout locally. The created electrons are captured and accelerated to relativistic energies by the strong electric fields associated with the plasma wake.

A 1.5 nC electron drive probe beam with a $\gamma = 20000$, a matched spot size of $\sim 1 \mu\text{m}$ and longitudinal length of 12.15 μm . The injection phase is determined so that no accelerating field acts on the probe beam while the focusing field is larger than zero and at its maximum value. The transverse (E_r and B_θ) and longitudinal wakefields (E_x), are related to each other through Panofsky-Wenzel theorem [31]. The experiment planned at FACET-II builds off the first successful demonstration of plasma photocathode at FACET [6]. The planned experiment will use an ionization laser pulse injected collinearly rather than perpendicular to the direction of beam propagation to generate ultracold electron beams.

There are unique challenges involved with simulating betatron radiation from this experiment. Simulating the beam ionization is beyond the capabilities of the Quasi-static PIC code used in model III B, and achieving the required resolution using EPOCH, required computational resources well exceeding our capabilities. In this experiment, the obtainable normalized emittance for the witness beam is at the single (μrad) scale. The plasma photo-cathode release a laser pulse which releases Helium

electrons and forms the trapped witness bunch. Plasma photocathodes generated ultrabright electron beams can drive X-ray free electron lasers close to the cold beam limit to produce coherent X-ray pulses of attosecond-Angstrom [32].

In contrast, the oscillating fields of the laser pulse do ionize both LIT and HIT media already at intensities orders of magnitude below the intensities needed to drive plasma waves. Here, the Ti: Sapphire release laser pulse with a duration is collinear with the electron bunch driver propagation axis and follows the electron bunch traveling to the right at a distance of approximately μm traveling to the right. A Trojan horse stage can act as a beam quality and brightness transformer. The incoming driver bunch is used to produce a witness bunch with a much higher brightness than the driver itself. Generally, there will always be a trade-off between bunch charge and emittance, and the optimum compromise may vary for different applications. Also, betatron radiation schemes are great since it is easy to produce and control betatron oscillations by releasing the HIT electrons off-axis. One should aim to optimize bunch compactness, charge, and emittance, while the energy spread of the electron bunch driver is of almost negligible importance. The Trojan horse scheme promises to generate tunable electron bunches with dramatically decreased emittance and increased brightness. Many diagnostic systems needed for characterizing the beam will be available at FACET-II. These include the betatron radiation spectrum via a Compton and pair spectrometer; the downstream beam imaging systems to determine phase space dilution of accelerated beams; and momentum-resolving spectrometers.

Angular spread diagnostics are useful ones that can separate the drive and witness spectra. The radiation analysis for the Trojan horse will be complicated because the generated witness beam will be low energy, and the radiation generated will be in a few keV ranges. However, this will not be an issue once the radiation is generated in the Trojan horse experiment. We can put detectors in a vacuum and outcouple the radiation using a spectrometer. Coherent synchrotron radiation will still be an issue, but we can use chicanes to minimize the effect. There will be a high correlation for the PWFA case. Adding compatibility with a new code is relatively simple. There are also disadvantages, as computational overhead is higher than more tightly integrated code. Tracking on multiple nodes, resuming from a progress file, and polar angular grid are also implemented to calculate the particle trajectories.

For the most accurate and computationally intensive model, we used the 3D PIC code OSIRIS [33] to generate particle trajectories which we input into the same LW code used with QuickPIC. Sampling a subset of particles from OSIRIS was more complicated than from QuickPIC because the former has variable-weighted particles. At the same time, the latter uses uniform particle weights, and the version of OSIRIS does not have built-in sampling

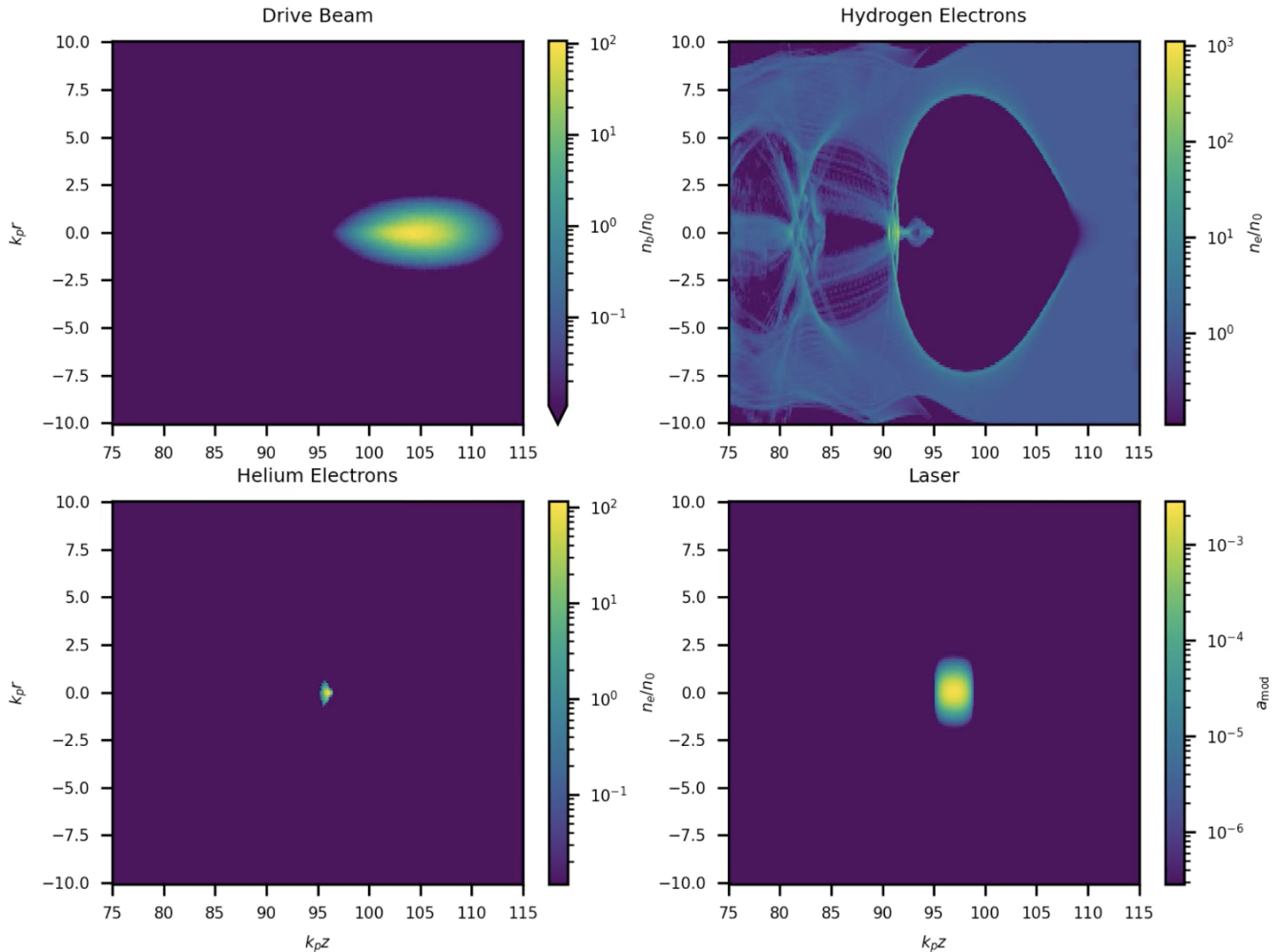


FIG. 5: Top left: Driver beam propagating through plasma shown on the top right. Bottom left: Generated witness beam using laser ionization, and the bottom right plot shows the dephasing of the laser.

functionality. In order to correctly sample, an initial simulation was performed where all the particles and weights used in the simulation were dumped, but very few output files were generated to prevent disk write bottlenecks and the generation of enormous data files. Next, particles are sampled with replacement, where the probability of sampling particle i is given by $p_i = w_i / \sum_j w_j$ where w_i is the weight of the i -th particle. After particles were sampled, redundantly sampled particles were combined by adding their weights. After this, a second simulation is run where the input file OSIRIS is instructed to only output particles with IDs in the list of sampled particles. The trajectories are computed from the output files, and the LW integral is computed using Eq. (11) and Eq. (12) where the \mathbf{V}_i are scaled by the square root of the particle weights.

A plasma profile comprising a vacuum section followed by an increasing short ramp section was implemented. One of the experimental goals of FACET-II is the demonstration of the creation of high brightness beams from a

‘Trojan horse’ plasma photocathode [34, 35]. This is a scheme in which a beam is created in a plasma wake through laser ionization of neutral gas. In this scheme, the target comprises both a high ionization threshold (HIT) gas and a low ionization threshold (LIT) gas. The LIT gas is preionized, and the drive beam creates a strong plasma wave blowout. OSIRIS does not output tags so we modified the OSIRIS code. Sampling is done with replacement and redundantly sampled macro particles combined. After modification in the code the particle tags were output to generate the trajectory data, and associated the trajectories with weights.

In Fig. 6 and Fig. 7, synchrotron radiation spectra for the driver beam are shown, and the spectrum is narrow. There are unique challenges involved with simulating betatron radiation from this experiment. Simulating the beam ionization is beyond the capabilities of the Quasi-static PIC code used in model IIIB, and achieving the required resolution using required computational resources well exceeding our capabilities. In recently pub-

Table III: Laser and electron beam parameters for Trojan horse experiment at FACET-II.

Parameter	Value
Species	H
Laser wavelength (nm)	800
Tau (fs)	50
Laser a_0	0.02
Plasma wavelength (μm)	250
$nH2(LIT) = nHe(HIT)$ (cm^{-3})	1.789e16
n_0 (cm^{-3})	1.79e16
ω_p (μm)	100
k_p^{-1} (μm)	39.79
Beam peak density	$9.3e23 = 52$
Drive beam parameter	Unit
E (GeV)	10
Q (nC)	-1.5
$Q\text{tilde}$	8.3
Ω_i	313
N	3.1×10^9
Laser beam waist (μm)	7
σ_x unmatched (μm)	4.5
σ_y unmatched (μm)	4.5
σ_z (μm)	12.15
$\epsilon_{n,x}$ (μm)	5
$\epsilon_{n,y}$ (μm)	5

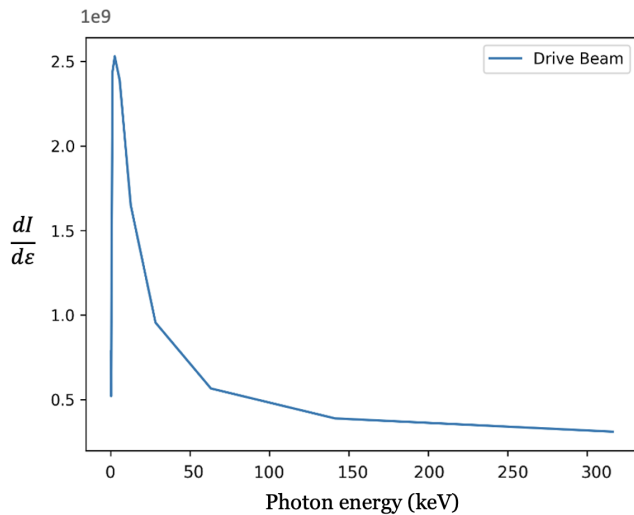


FIG. 6: Photon energy spectrum of the radiation emitted by the driver bunch computed using OSIRIS and LW code.

lished paper [36], algorithm characterize electromagnetic waves by implementing the LW potentials to extract radiation emission. We compared our model with OSIRIS Radio code and results are similar.

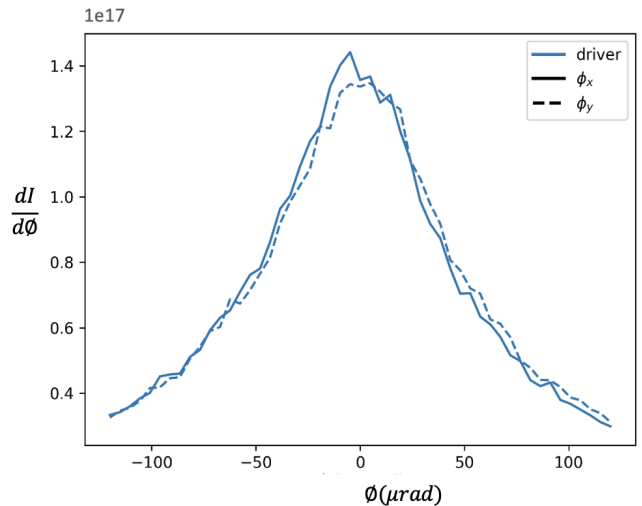


FIG. 7: 1-D angular ϕ_x and ϕ_y distribution of betatron radiation generated by driver beam.

D. Benchmark using full Particle-in-Cell EPOCH with Monte Carlo QED radiation

Despite the sophistication of the PIC and LW radiation models, some effects still require a higher level of sophistication to simulate. Monte Carlo QED radiation models treat high-energy photons as discrete particles, and electrons have some probability of emitting them. Statistical properties of the photons could matter, especially at extremely high energies, quantum recoil, statistical properties, and strong field effects. An example is EPOCH, a 3D fully explicit PIC code that uses a Monte Carlo QED model to simulate radiation generation [37, 38].

We found that accurately simulating radiation using this method exceeded our computational resources. A primary challenge with 3D explicit codes is the artificial slow-down of the speed of light on a finite difference time domain (FDTD) grid. This means, for example, that a relativistic electron propagating along a straight line with constant velocity in free space will nonphysically emit numerical Cherenkov radiation (NCR) at wavelengths corresponding to the grid cell size and may even grow as an instability by imprinting into the current profile [39]. In EPOCH, we use a dispersion-reduced FDTD solver [40] and an 8-point, compensated [41] linear current filter to mitigate this effect. Such schemes are imperfect and can slightly alter the Fourier content of fields at the grid resolution. However, the radiation model in EPOCH is photon-based, not field-based, and the emitted radiation wavelengths are well beyond the grid resolution. Therefore, we expect minimal interference from the smoothing filter and microscopic details of the dispersion on our results while retaining the benefit of smooth fields to be used in QED calculations. One of the primary challenges associated with using EPOCH is that extensive computational resources are needed to correctly resolve physically

relevant length scales, especially in the matched beam case when the beam spot size is small. The domain is set up with $512 \times 512 \times 512$ cells per in the longitudinal and transverse directions, allowing the minor features in those directions to be resolved. Drive and witness beams in the plasma are represented with macro-particles per cell, assuming an immobile neutralizing background.

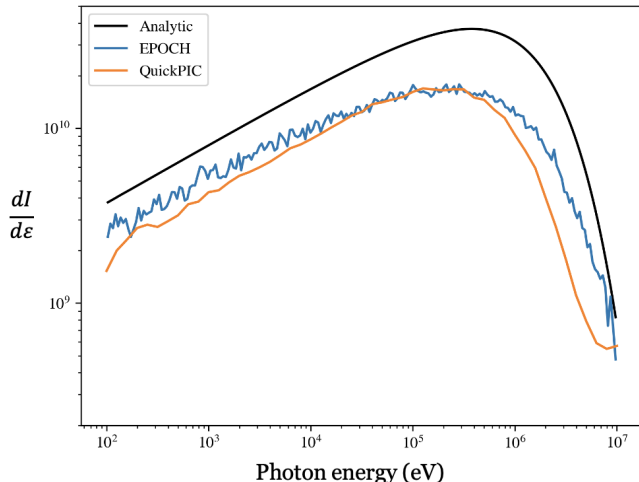


FIG. 8: Benchmark of photon energy spectrum of the radiation emitted by the driver bunch computed using EPOCH code, analytic and QuickPIC code. In the analytic plot the energy loss of the drive beam is not considered.

EPOCH is the most sophisticated and computationally intensive betatron radiation model. In EPOCH input files, a smoothing function is applied to the current generated during the particle push. It helps to reduce noise and self-heating in a simulation. It can be substantially tuned to damp high frequencies in the currents and can be used to reduce the effect of NCR. Once we turn on the current filtering, we can set the following keys: smooth iterations, integer number of iterations of the smoothing function to be performed. If not present defaults to one iteration, more iterations will produce smoother results but will be slower. In Fig. 8 benchmark of photon energy spectrum of the radiation emitted by the driver bunch computed using EPOCH code, analytic and QuickPIC code. The analytical curve is much higher than the EPOCH and QuickPIC as the analytic plot does not consider the energy loss of the drive beam. However this would not be an issue in the case of witness beam which is more stable or beams with zero emittances.

Gamma rays emitted from the betatron radiation process in underdense plasma wakefields and high field-laser-induced Compton scattering produce unique experimental signatures which can reveal interaction physics at the challenging ultra-short spatial and temporal experimental scales. Additionally, radiative diagnostics provide a non-intercepting, non-destructive probe of the extreme high-field environments relevant to advanced acceleration

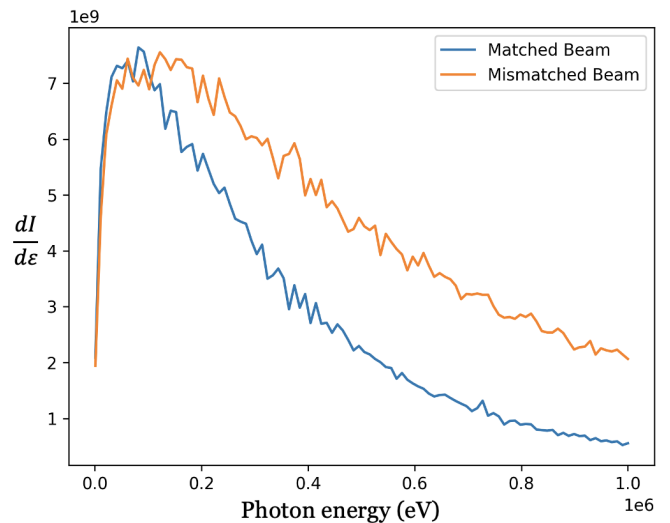


FIG. 9: Photon energy spectrum of the radiation emitted by the driver bunch computed using EPOCH code for matched and mismatched beam at the plasma entrance.

techniques. An electron beam is matched to the plasma density if the beam envelope experiences no oscillations. In Fig. 9, the emitted radiations from a matched and mismatched beams are plotted in orange and blue colour, respectively. Higher photon energy is achieved in the unmatched case because of the high oscillation amplitudes of the electrons.

IV. FACET-II PWFA SIMULATIONS

This section introduces a parameter set for a PWFA at FACET-II. The simulation parameters were summarized in Table II. We characterized the radiation for the parameter set based on what is feasible for PWFA experiments at FACET-II. We demonstrated the effect caused by focusing and defocusing at betatron periods. Scalloping in the driver beam's head results in deterioration of the beam after a few centimeters, propagation in plasma.

We are simulating two bunch scenario of drive and witness in PWFA. The initial emittance of the drive beam was $3.2 \mu\text{m}$ and $3 \mu\text{m}$ in the x and y directions, respectively. However, the energy spread in the driver beam is significantly less; hence the emittance is not growing fast. The centroid oscillations in x and y are different because the emittance is different in both directions. The drive beam starts at a spot size of $5 \mu\text{m}$ and focuses down to $1 \mu\text{m}$ because of the linear forces. The initial energy of the driver beam is 10 GeV, after propagating for a distance of $z = 30 \text{ cm}$, the beam loses approximately 0.8 GeV energy to the plasma electrons. As the ramp profile is semi-Gaussian, the driver beam decelerates quickly at lower plasma densities and maintains a 4 GeV/m decelerating gradient for a uniform plasma density.

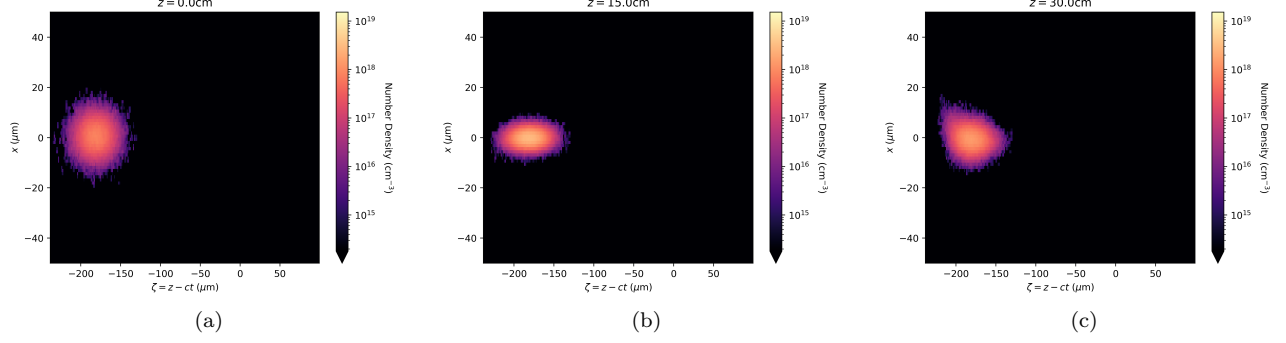


FIG. 10: Beam electron number density x-z (a) slices at $z = 0$ cm, (b) slices at $z = 15$ cm, (c) slices at $z = 30$ cm.

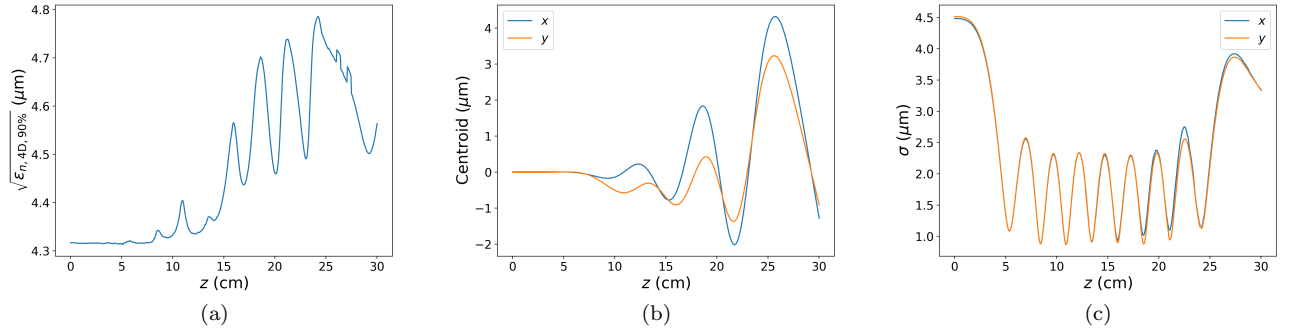


FIG. 11: (a) Witness beam emittance growth over a long propagation distance, (b) witness beam centroid and (c) is the witness sigma evolution.

In Fig. 10 witness beam electron number density x-z slices at (a) $z = 0$ cm, (b) $z = 15$ cm, (c) $z = 30$ cm are shown. The witness beam is more stable than the driver beam because it is in the pure ionic column. The witness beam oscillates at a betatron frequency, and the oscillations will lead to betatron radiation. In Fig. 11(a) witness beam emittance growth over a longer propagation distance is plotted. We notice that the witness beams 90% emittance grows very little. The growth at longer propagation is much less than the driver beam because the witness beam is more stable and not deteriorating like the driver. In Fig. 11(b) the witness beam centroid is plotted. The centroid oscillation amplitude change in the x and y directions is the same. In 11(c) witness sigma evolution is shown; the beam starts at $4.5 \mu\text{m}$ and focuses down to $0.8 \mu\text{m}$. The beam oscillates at a betatron frequency, where it focuses and defocuses.

In Fig. 12(a) the energy gain in the witness beam is plotted for a length at the entrance of plasma ($z=0$), cm, the beam energy increase to more than 11 GeV. Figure 12(b) shows that the accelerating gradient over a ramp plasma profile is 7 GeV/m. The witness beam's accelerating gradient is much less on the up and down ramp when the plasma densities are smaller, but it gradually increases with the plasma density. In Fig. 12(c), we show

the energy spread in the witness beam. The spectrum of radiation produced by the drive, witness, and both beams are shown in Fig. 13. The noise in the spectrum is primarily a result of the finite ϕ_x/ϕ_y step size. In this case, the energy of the drive and witness beams are 10 GeV each. The separation between the two beams is $150 \mu\text{m}$. The maximum share of the radiation is produced by the witness beam, which helps diagnosing witness beam parameters. We notice that the high energy tail of the radiation is dominated by the witness beam.

V. RADIATION PRODUCED BY DRIVE BEAM IN TROJAN HORSE EXPERIMENT

One of the experimental goals of FACET-II is the demonstration of high-brightness beams generated from a Trojan horse plasma photocathode [34, 35]. In this scheme, a beam is created within a plasma wakefield, through laser ionization of neutral gas. The gaseous mixture is comprised of a low ionization threshold species for plasma wakefield generation, and a high ionization threshold species for particle generation. Another way of generating witness beam using laser and beam radial fields overlap to liberate electrons from the tunneling ion-

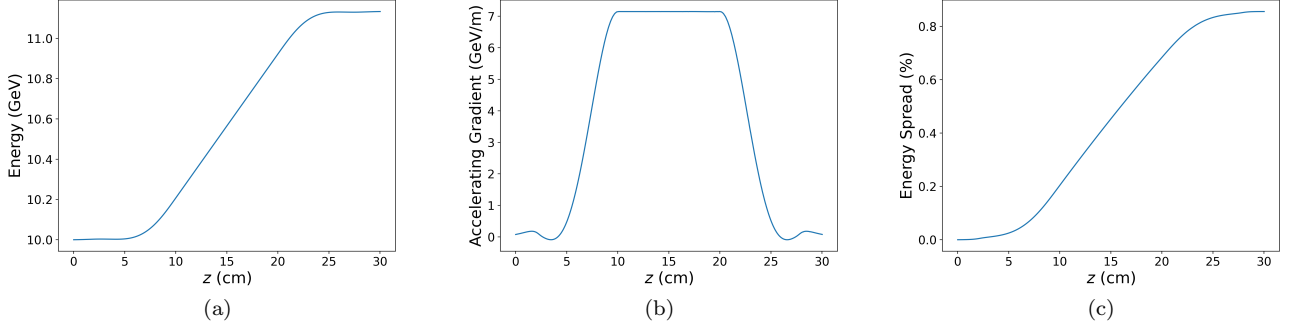


FIG. 12: (a) Energy gain in witness beam, (b) accelerating gradient over a ramp plasma profile and (c) energy spread in the witness beam.

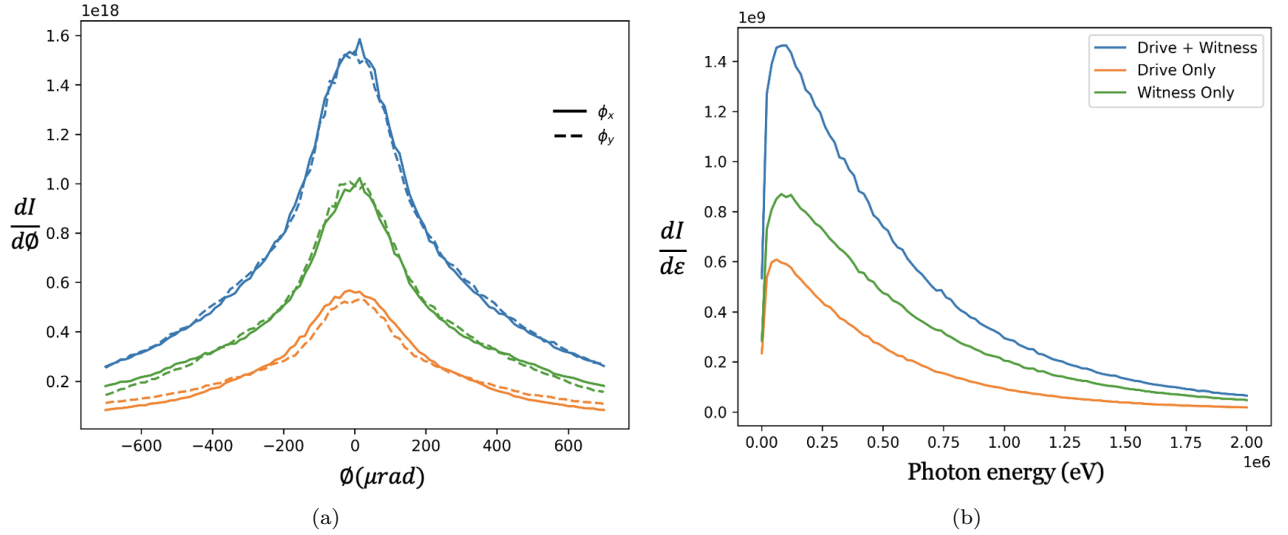


FIG. 13: (a) 1-D angular distribution of betatron radiation generated by driver and witness beam (b) betatron radiation spectrum from the prototype simulation for both the beams charge is 1.5 nC.

ization of the non ionized gas species is discussed in [42]. In this section, we simulated a single bi-Gaussian beam traveling through a uniform plasma using the Quasi-static PIC code QuickPIC [27, 28] for the FACET-II E-310 Trojan horse parameters. The beam driver is assumed to have a bi-Gaussian density profile,

$$n_b(\xi, r)/n_0 = (n_b/n_0) e^{-\xi^2/(2\sigma_\xi^2)} e^{-r^2/(2\sigma_r^2)} \quad (13)$$

where $\xi \equiv z - ct$ is the beam co-moving coordinate, c is the speed of light in vacuum, $n_b \equiv (Q/e)/[(2\pi)^{3/2}\sigma_\xi\sigma_r^2]$ is the peak beam-density, n_0 is the plasma electron density, Q is the beam charge and σ_ξ , σ_r are the beam longitudinal and radial RMS sizes, respectively. The beam has initial kinetic energy E_{k0} , and energy spread $\delta E_{k0}/E_{k0} = 1\%$. The simulation parameters are shown in Table III.

Fig. 14(a) shows the PIC simulation snapshots of the

blowout at $z = 12.5$ cm. The driver beam is dense enough to eject all the plasma electrons to form a strong blowout. In Fig. 14(b) 1-D angular ϕ_x and ϕ_y distribution of betatron radiation and, Fig. 14(c) photon energy spectrum of the radiation emitted by the driver bunch computed using model III B. We measure the angular information about the photons, critical for understanding the upstream physics, via their lateral displacement. Further information is obtained from double differential information (angular and spectral) to assess beam dynamics and constrain modeling of plasma beam dynamics, in Trojan horse injection experiment.

The ideal spectrum shown in Fig. 14(c) is peaked in the range 20-75 keV. The spectrum extends, however, to the 2 MeV range which is approached using gamma spectrometer. The total number of photons is E10, and occupy mrad in divergence angle, as illustrated in differential spectra shown in Fig. 14(b). It should be noted

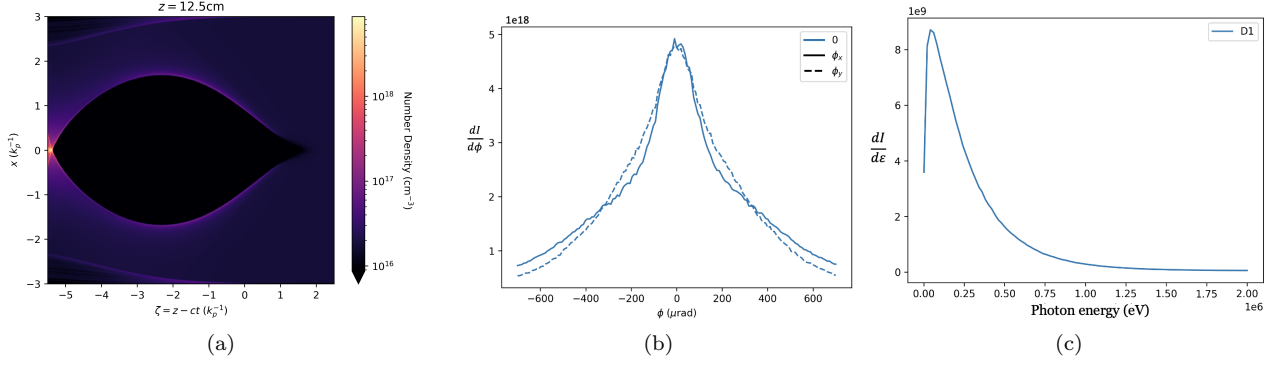


FIG. 14: (a) PIC simulation snapshots of the blowout at $z = 12.5$ cm, (b) 1D angular ϕ_x and ϕ_y distribution of betatron radiation generated by driver beam using QuickPIC simulations and, (c) photon energy spectrum of the radiation emitted by the driver bunch computed using QuickPIC and LW code.

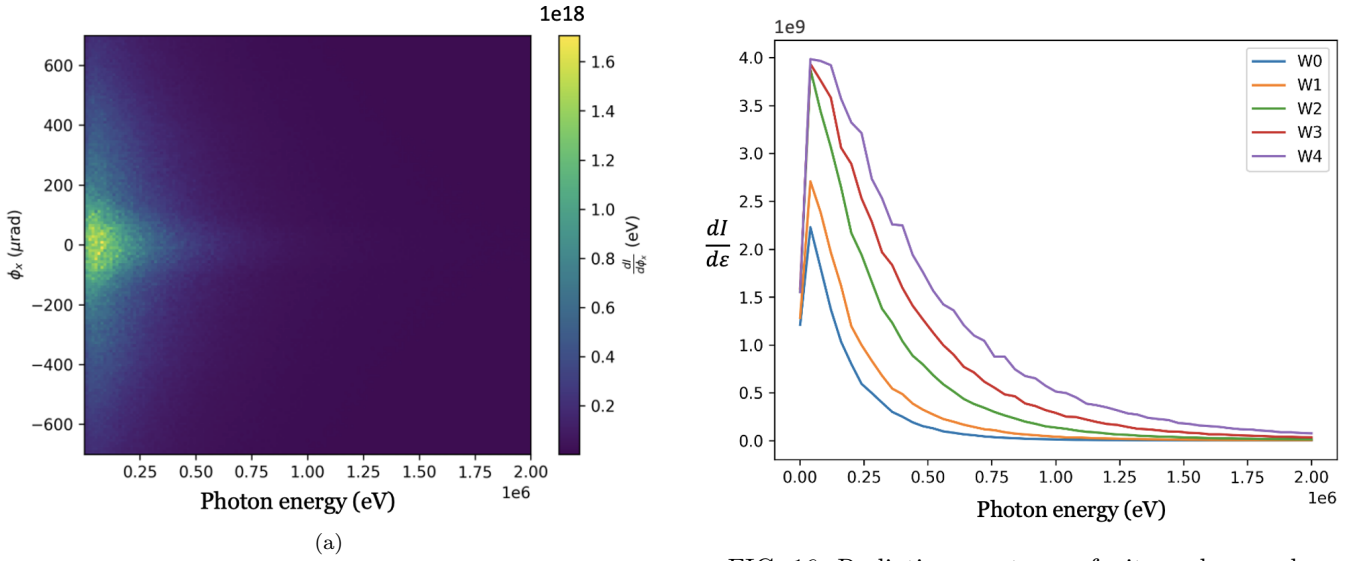


FIG. 15: Betatron radiation angular distributions emitted by the drive bunch.

FIG. 16: Radiation spectrum of witness beam when beam is offset for few different cases.

that the spectrum will extend to higher photon energy in the case of larger emittance beams, as foreseen in initial runs at FACET-II.

In Fig. 15(a), betatron radiation angular distribution and Fig. 15(b) double differential distributions emitted by the drive bunch are shown. There is a spike at the centre as most of the high energy photons are emitted at smaller angles. Simulations were done for studying different witness offsets effects on the radiation spectrum. In Fig. 16 a witness beam offset from the axis shows distinct betatron radiation signatures. Several simulations were ran using model III B, where the witness beam's x centroid was offset by a value Δx . The values of Δx scanned over were $0\mu m$, $5\mu m$, $10\mu m$, $15\mu m$, and $20\mu m$. The $\Delta x = 0$ simulation is the on axis simulation.

The trailing bunch should be smaller in the longitudinal direction than the drive beam in plasma for loading the wake, and it must contain sufficient charge which can

Table IV: Radiation emitted by drive, witness and both beams in PWFA for different witness offsets.

Simulation	Offsets (μm)	Witness energy (eV)
W0	0	4.380e+21
W1	5	6.678e+21
W2	10	1.215e+22
W3	15	1.659e+22
W4	20	2.163e+22

flatten the wake so that the energy spread will be narrow. The drive beam dynamics in these simulations are unchanged. The witness beam dynamics were similar except for two main differences: beams with a larger offset had more emittance growth and x spot size growth. The large offset beams lost some charge, although, for the very most significant offset, it was only 1.21%. Large offset beams had a slightly smaller energy spread with the $\Delta x = 20\mu m$ case having $\Delta\gamma/\gamma \approx 0.711\%$ compared to the $\Delta x = 0\mu m$ case which had $\Delta\gamma/\gamma \approx 0.856\%$. In Fig. 16 spectrum has many variations depending on different offsets of the witness beam. Electrons oscillate at larger amplitudes when witness beam has the highest offset.

VI. OUTLOOK AND FUTURE GOALS

We used different techniques to compute the motion of charged particles, including analytical methods, numerical methods, PIC method, Monte Carlo simulation, and hybrid methods, where we combined two or more of the above techniques to take advantage of their strengths and overcome limitations. We compared and validated our code against the analytic expressions under certain conditions with zero emittance, finite emittance, and matched spot size. We also minimized witness beam acceleration by placing at wakefields zero crossing and the time evolution of the drive beam was turned off.

Model III A is primarily helpful for big data sets. Model III B is well-suited for all the FACET-II related experiments and other beam-driven plasma physics because it tells us the exact beam plasma interaction dynamics and radiation emitted. Model III C calculates radiation by obtaining trajectories from the full PIC code OSIRIS. We benchmark our codes with EPOCH III D which calculates radiation using QED modules that requires information about generated photons. Experimentally analyzing witness beam parameters from betatron radiation is challenging in cases where the drive beam produces most of the radiation. The total radiation emitted by a beam scales as $I_{b,0} \sim Q\gamma^2\sigma_{\perp}^2$, this is less of an issue for witness beams that have higher charges, larger spot sizes, or higher energies. However our models works well for both higher and lower charge beams.

The full spectrum of betatron radiation produced by the electron beams in the plasma source could be measured using above discussed models. The combined spectral and angular photon spectral yield can provide an in-

direct measurement of the beam's phase space distribution while inside the plasma, which is critical to fully understanding and ultimately optimizing the beam dynamics inside a PWFA in order to produce high-brightness beams for high energy physics applications. It may also be used to detect deviations from ideal focusing conditions in the plasma, such as what might arise from ion collapse, a potentially severe problem for linear collider beams in a PWFA. Beyond observation and optimization, one may actively seek microscopic control over the beam. As proposed at UCLA, an example is the resonant excitation of betatron oscillations [43] via an undulator magnet superimposed on a plasma channel. This amplitude dependence may permit the determination of the beam emittance through a complete frequency spectrum measurement.

If the oscillations are small ($K_u < 1$), then one may exploit beam matching condition to measure the emittance. With a Gaussian transverse phase space amplitude distribution assumed, the summation over amplitudes produces an RMS normalized emittance that is remarkably related to the RMS spectral width as $\Delta\lambda_{rms} = 2\varepsilon_{rms,n}/\gamma$. If one attempts to measure this spectral width, it is implicit that the radiation emitted should be collected at constant energy (γ). This requires a significant length of beam-plasma interaction where ion focusing is present while the acceleration is not. This situation can be obtained using an appropriate plasma profile.

Relevant energies for FACET-II PWFA experiments extend roughly from 1 to 10 GeV, while the plasma density is chosen most often near 10^{18}cm^{-3} . The relevant photon energies that may be encountered thus range from a few keV to the MeV level, and this must be accommodated through a spectrometer and detector design. It is expected that these γ -rays will originate from high-energy beams, like the drive beam, that experience a high K_u inside the plasma. For high K_u , the spectrum of an individual electron follows a synchrotron-like distribution. Therefore, one must tie the amplitudes to the distribution of critical energies to deduce the emittance through the spectrum. The angular dependence of the spectrum is related to the beam dynamics inside the plasma. For example, an on-axis symmetric bunch performing mismatched oscillations in the plasma will lead to betatron radiation with much higher critical energy in the center than on the side of the photon beam. However, if the beam is matched, there is no correlation between the angle and spectrum in the very high K_u limit. The double differential spectrum can provide simultaneous information regarding matching and betatron amplitudes, which then, in turn, allow constraints on the transverse phase space, particularly the beam emittance. In general, because bunch asymmetries and asynchronous x and y oscillations impact the double differential spectrum, it is essential to rely on LW simulations to interpret and deduce beam parameters and phase space.

Betatron radiation will be an invaluable tool for the

diagnostics of upcoming experiments at FACET-II with mobile ions. In these experiments, a long bright beam causes the ions in the blowout bubble to collapse toward the axis producing an ion column [44]. The strong focusing fields resulting from this will generate large amounts of high-energy betatron radiation. This will lead to a prominent and unique radiation signature that can be used to diagnose the beam-plasma interaction. A flat beam ion motion experiment can demonstrate the formation of an asymmetric beam-ion equilibrium at FACET and AWA. The beam becomes a complex, non-Gaussian distribution due to phase space mixing due to the non-linear fields, which are a consequence of ion motion. The collisionless relaxation to equilibrium can be seen in the beam spot size and emittance evolution. The scientific goal of the project is to model codes that can calculate radiation given the information of the particle trajectories for any available beam facilities and then use that radiation spectrum to reconstruct the beam parameters using machine learning algorithms. A complete set of theoretical, computational, and experimental knowledge required for calculating the betatron radiation spectrum is presented.

Recent calculations[45] have predicted that a high-density ($n_b > 3 \times 10^{19} \text{ cm}^{-3}$) ultra-relativistic electron beam passing through a millimeter-thick conductor produces bright collimated gamma-ray pulses at high electron-to-photon energy conversion efficiencies, up to 60%. This emission occurs by synchrotron radiation in the presence of beam filamentation rather than ordinary bremsstrahlung. In this collective phenomenon, characterization of both the angular and spectral properties of the gamma-ray burst at the onset of the beam-filamentation instability is of critical importance. At FACET-II, the E-305 experiment “Beam filamentation and bright gamma-ray bursts” will study this phenomenon.

The needs for the FACET-II E-300 collaboration for measuring beam matching are to be able to interpret the integrated signal to reach the conditions suitable for emittance preservation, the critical goal of this experiment. There is a strong correlation between minimizing the emittance growth and observed minimization of the integrated betatron radiation signal. This relationship arises due to the additional radiation emitted when the

beam is mismatched.

The radiation diagnostics could also be used in future PWFA-based scenarios for linear collider, where beams with highly asymmetric emittance are expected. Therefore, betatron radiation diagnostic systems are one among those needed for characterizing the beam and will be available at FACET-II. These include the betatron radiation spectrum via a Compton or pair spectrometer, as described in [46, 47]; the downstream beam imaging systems to determine phase space dilution of accelerated beams in this case, and momentum resolving spectrometers. Betatron radiation models promise functional diagnostics for understanding the beam and plasma interaction dynamics. In addition, betatron radiation will be helpful for the dragon tail experiment at FACET-II [42]. The generated witness beam and the driver beam will produce a betatron radiation signal which can be characterized using above mention betatron models. Once established, the beam-plasma interaction can be interrogated by measuring the betatron radiation spectrum for resonantly excited plasma wakefields in the quasi-nonlinear(QNL) regime. In all of the experiments present at FACET-II, the expected photon spectra will be quite broad, with the exception of the small emittance injected beam in Trojan horse-like scenarios. We developed robust methods of taking the observed distributions, of the types described in the previous section, to invert the spectral information discussed in [18]. This is done using machine-learning algorithms and MLE. This approach requires that the algorithms pick out established patterns in the data.

VII. ACKNOWLEDGEMENT

This work was performed with the support of the US Department of Energy, Division of High Energy Physics, under Contract No. DE-SC0009914, and the STFC Liverpool Centre for Doctoral Training on Data Intensive Science (LIV.DAT) under grant agreement ST/P006752/1. This work used computational and storage services associated with the SCARF cluster, provided by the STFC Scientific Computing Department, United Kingdom.

-
- [1] I. Blumenfeld et. al, Energy doubling of 42 gev electrons in a metre-scale plasma wakefield accelerator, *Nature* **445**, 741 (2007).
- [2] M. J. Hogan, T. O. Raubenheimer, A. Seryi, P. Muggli, T. Katsouleas, C. Huang, W. Lu, W. An, K. A. Marsh, W. B. Mori, C. E. Clayton, and C. Joshi, Plasma wakefield acceleration experiments at FACET, *New Journal of Physics* **12**, 055030 (2010).
- [3] M. Litos et.al, High-efficiency acceleration of an electron beam in a plasma wakefield accelerator, *Nature* **515**, 92 (2014).
- [4] M. Litos, E. Adli, J. M. Allen, W. An, C. I. Clarke, S. Corde, C. E. Clayton, J. Frederico, S. J. Gessner, S. Z. Green, M. J. Hogan, C. Joshi, W. Lu, K. A. Marsh, W. B. Mori, M. Schmeltz, N. Vafaei-Najafabadi, and V. Yakimenko, 9 GeV energy gain in a beam-driven plasma wakefield accelerator, *Plasma Physics and Controlled Fusion* **58**, 034017 (2016).
- [5] S. Corde, E. Adli, J. M. Allen, W. An, C. I. Clarke, C. E. Clayton, J. P. Delahaye, J. Frederico, S. Gessner, S. Z.

- Green, M. J. Hogan, C. Joshi, N. Lipkowitz, M. Litos, W. Lu, K. A. Marsh, W. B. Mori, M. Schmeltz, N. Vafaei-Najafabadi, D. Walz, V. Yakimenko, and G. Yocky, Multi-gigaelectronvolt acceleration of positrons in a self-loaded plasma wakefield, *Nature* **524**, 442 (2015).
- [6] A. Deng *et al.*, Generation and acceleration of electron bunches from a plasma photocathode, *Nature Physics* **15**, 1156 (2019).
- [7] V. Yakimenko, L. Alsberg, E. Bong, G. Bouchard, C. Clarke, C. Emma, S. Green, C. Hast, M. J. Hogan, J. Seabury, N. Lipkowitz, B. O'Shea, D. Storey, G. White, and G. Yocky, Facet-ii facility for advanced accelerator experimental tests, *Phys. Rev. Accel. Beams* **22**, 101301 (2019).
- [8] C. Joshi, E. Adli, W. An, C. E. Clayton, S. Corde, S. Gessner, M. J. Hogan, M. Litos, W. Lu, K. A. Marsh, W. B. Mori, N. Vafaei-Najafabadi, B. O'shea, X. Xu, G. White, and V. Yakimenko, Plasma wakefield acceleration experiments at FACET II, *Plasma Physics and Controlled Fusion* **60**, 034001 (2018).
- [9] C. Emma, A. Edelen, M. J. Hogan, B. O'Shea, G. White, and V. Yakimenko, Machine learning-based longitudinal phase space prediction of particle accelerators, *Phys. Rev. Accel. Beams* **21**, 112802 (2018).
- [10] A. Scheinker, S. Gessner, C. Emma, and A. L. Edelen, Adaptive model tuning studies for non-invasive diagnostics and feedback control of plasma wakefield acceleration at facet-ii, *Nuclear Instruments and Methods in Physics Research Section A: Accelerators, Spectrometers, Detectors and Associated Equipment* **967**, 163902 (2020).
- [11] C. Emma, A. Edelen, A. Hanuka, B. O'Shea, and A. Scheinker, Virtual diagnostic suite for electron beam prediction and control at facet-ii, *Information* **12**, 10.3390/info12020061 (2021).
- [12] E. Esarey *et al.*, "synchrotron radiation from electron beams in plasma-focusing channels", *Phys. Rev. E* **65**, 056505 (2002).
- [13] S. Corde, K. Ta Phuoc, G. Lambert, R. Fitour, V. Malka, A. Rousse, A. Beck, and E. Lefebvre, Femtosecond x rays from laser-plasma accelerators, *Rev. Mod. Phys.* **85**, 1 (2013).
- [14] I. Kostyukov, S. Kiselev, and A. Pukhov, X-ray generation in an ion channel, *Physics of Plasmas* **10**, 4818 (2003), <https://doi.org/10.1063/1.1624605>.
- [15] Y. Sakai *et al.*, "single shot, double differential spectral measurements of inverse compton scattering in the nonlinear regime", *Phys. Rev. Accel. Beams* **20**, 060701 (2017).
- [16] B. Williamson, G. Xia, S. Gessner, A. Petrenko, J. Farmer, and A. Pukhov, Betatron radiation diagnostics for awake run 2, *Nuclear Instruments and Methods in Physics Research Section A: Accelerators, Spectrometers, Detectors and Associated Equipment* **971**, 164076 (2020).
- [17] L. Liang, G. Xia, H. Saberi, J. P. Farmer, and A. Pukhov, *Simulation study of betatron radiation in awake run 2 experiment* (2022).
- [18] M. Yadav, S. Zhang, M. Oruganti, B. Naranjo, Y. Zhuang, . Apsimon, C. P. Welsch, and J. B. Rosenzweig, *Reconstruction of electron radiation spectra and beam parameters from photon spectrometer data in accelerator experiments using machine learning* (2022).
- [19] Y. Zhuang, B. Naranjo, J. Rosenzweig, and M. Yadav, Spectral reconstruction for facet-ii compton spectrometer, in *Proc. IPAC'21*, International Particle Accelerator Conference No. 12 (JACoW Publishing, Geneva, Switzerland, 2021) pp. 4346–4348, <https://doi.org/10.18429/JACoW-IPAC2021-THPAB273>.
- [20] M. Yadav *et al.*, Physical aspects of collinear laser injection at slac facet-ii e-310: Trojan horse experiment, in *Proc. IPAC'22*, International Particle Accelerator Conference No. 13 (JACoW Publishing, Geneva, Switzerland, 2022) pp. 1787–1790.
- [21] M. Yadav, C. Hansel, Y. Zhuang, B. Naranjo, N. Majernik, A. Perera, Y. Sakai, G. Andonian, O. Williams, P. Manwani, J. Resta-Lopez, O. Apsimon, C. Welsch, B. Hidding, and J. Rosenzweig, Modeling betatron radiation diagnostics for e-310 – trojan horse (2021), [arXiv:2107.00483 \[physics.acc-ph\]](https://arxiv.org/abs/2107.00483).
- [22] M. Oruganti, B. Naranjo, J. Rosenzweig, and M. Yadav, Comparing Methods of Recovering Gamma Energy Distributions from PEDRO Spectrometer Responses, *JACoW IPAC2022, WEPOST040* (2022).
- [23] M. Ritsch-Marte, Orbital angular momentum light in microscopy, *Philosophical Transactions of the Royal Society A: Mathematical, Physical and Engineering Sciences* **375**, 20150437 (2017), <https://royalsocietypublishing.org/doi/pdf/10.1098/rsta.2015.0437>.
- [24] J. B. Rosenzweig, B. Breizman, T. Katsouleas, and J. J. Su, Acceleration and focusing of electrons in two-dimensional nonlinear plasma wake fields, *Phys. Rev. A* **44**, R6189 (1991).
- [25] J. B. Rosenzweig, A. M. Cook, A. Scott, M. C. Thompson, and R. B. Yoder, Effects of ion motion in intense beam-driven plasma wakefield accelerators, *Physical Review Letters* **95**, 10.1103/physrevlett.95.195002 (2005).
- [26] A. Hofmann, *The Physics of Synchrotron Radiation*, Cambridge Monographs on Particle Physics, Nuclear Physics and Cosmology (Cambridge University Press, 2004).
- [27] C. Huang, V. Decyk, C. Ren, M. Zhou, W. Lu, W. Mori, J. Cooley, T. Antonsen, and T. Katsouleas, QUICKPIC: A highly efficient particle-in-cell code for modeling wakefield acceleration in plasmas, *Journal of Computational Physics* **217**, 658 (2006).
- [28] W. An, V. K. Decyk, W. B. Mori, and T. M. Antonsen, An improved iteration loop for the three dimensional quasi-static particle-in-cell algorithm: QuickPIC, *Journal of Computational Physics* **250**, 165 (2013).
- [29] P. S. M. Claveria *et al.*, "betatron radiation and emittance growth in plasma wakefield accelerators", *Philosophical Transactions of the Royal Society A: Mathematical, Physical and Engineering Sciences* **377**, 20180173 (2019).
- [30] E. Parra, S. J. McNaught, and H. M. Milchberg, Characterization of a cryogenic, high-pressure gas jet operated in the droplet regime, *Review of Scientific Instruments* **73**, 468 (2002), <https://doi.org/10.1063/1.1433945>.
- [31] E. Esarey, C. B. Schroeder, and W. P. Leemans, Physics of laser-driven plasma-based electron accelerators, *Rev. Mod. Phys.* **81**, 1229 (2009).
- [32] A. F. Habib, G. G. Manahan, P. Scherkl, T. Heinemann, A. Sutherland, R. Altuiri, B. M. Alotaibi, M. Litos, J. Cary, T. Raubenheimer, E. Hemsing, M. J. Hogan, J. B. Rosenzweig, P. H. Williams, B. W. J. McNeil, and B. Hidding, Attosecond-angstrom free-electron-laser to-

- wards the cold beam limit, *Nature Communications* **14**, 1054 (2023).
- [33] R. Fonseca *et al.*, Osiris: A three-dimensional, fully relativistic particle in cell code for modeling plasma based accelerators (2002) pp. 342–351.
- [34] B. Hidding, G. Pretzler, J. B. Rosenzweig, T. Königstein, D. Schiller, and D. L. Bruhwiler, Ultracold electron bunch generation via plasma photocathode emission and acceleration in a beam-driven plasma blowout, *Phys. Rev. Lett.* **108**, 035001 (2012).
- [35] G. G. Manahan, A. F. Habib, P. Scherkl, D. Ullmann, A. Beaton, A. Sutherland, G. Kirwan, P. Delinikolas, T. Heinemann, R. Altuijri, A. Knetsch, O. Karger, N. M. Cook, D. L. Bruhwiler, Z.-M. Sheng, J. B. Rosenzweig, and B. Hidding, Advanced schemes for underdense plasma photocathode wakefield accelerators: pathways towards ultrahigh brightness electron beams, *Philosophical Transactions of the Royal Society A: Mathematical, Physical and Engineering Sciences* **377**, 20180182 (2019).
- [36] M. Pardal, A. Sainte-Marie, A. Reboul-Salze, R. Fonseca, and J. Vieira, Radio: An efficient spatiotemporal radiation diagnostic for particle-in-cell codes, *Computer Physics Communications* **285**, 108634 (2023).
- [37] T. D. Arber, K. Bennett, C. S. Brady, A. Lawrence-Douglas, M. G. Ramsay, N. J. Sircombe, P. Gillies, R. G. Evans, H. Schmitz, A. R. Bell, and C. P. Ridgers, Contemporary particle-in-cell approach to laser-plasma modelling, *Plasma Physics and Controlled Fusion* **57**, 113001 (2015).
- [38] C. Ridgers, J. Kirk, R. Duclous, T. Blackburn, C. Brady, K. Bennett, T. Arber, and A. Bell, Modelling gamma-ray photon emission and pair production in high-intensity laser-matter interactions, *J. Comput. Phys.* **260**, 273 (2014).
- [39] A. D. Greenwood, K. L. Cartwright, J. W. Luginsland, and E. A. Baca, On the elimination of numerical cerenkov radiation in pic simulations, *J. Comput. Phys.* **201**, 665684 (2004).
- [40] R. Lehe, A. Lifschitz, C. Thaury, V. Malka, and X. Davoine, Numerical growth of emittance in simulations of laser-wakefield acceleration, *Phys. Rev. ST Accel. Beams* **16**, 021301 (2013).
- [41] J.-L. Vay and B. B. Godfrey, Modeling of relativistic plasmas with the particle-in-cell method, *Comptes Rendus Mcanique* **342**, 610 (2014).
- [42] P. Manwani, D. Bruhwiler, B. Hidding, M. Litos, N. Majernik, and J. Rosenzweig, High Brightness Electron Beams from Dragon Tail Injection and the E-312 Experiment at FACET-II, in *Proc. IPAC'21*, International Particle Accelerator Conference No. 12 (JACoW Publishing, Geneva, Switzerland, 2021) pp. 1728–1731, <https://doi.org/10.18429/JACoW-IPAC2021-TUPAB146>.
- [43] N. Majernik and J. Rosenzweig, Resonant excitation of betatron oscillations, *Nuclear Instruments and Methods in Physics Research Section A: Accelerators, Spectrometers, Detectors and Associated Equipment* **865**, 91 (2017), physics and Applications of High Brightness Beams 2016.
- [44] C. Hansel, M. Yadav, P. Manwani, W. An, W. Mori, and J. Rosenzweig, *Plasma wakefield accelerators with ion motion and the e-314 experiment at facet-ii* (2021).
- [45] A. Benedetti, M. Tamburini, and C. H. Keitel, Giant collimated gamma-ray flashes, *Nat. Photonics* **12**, 319 (2018).
- [46] B. Naranjo *et al.*, Compton spectrometer for facet-ii, in *Proc. IPAC'21*, International Particle Accelerator Conference No. 12 (JACoW Publishing, Geneva, Switzerland, 2021) pp. 4332–4335, <https://doi.org/10.18429/JACoW-IPAC2021-THPAB269>.
- [47] B. Naranjo, G. Andonian, N. Cavanagh, A. Di Piazza, A. Fukasawa, E. Gerstmayr, R. Holtzapple, C. Keitel, N. Majernik, S. Meuren, C. Nielsen, M. Oruganti, D. Reis, J. B. Rosenzweig, Y. Sakai, G. Sarri, D. Storey, O. Williams, M. Yadav, and V. Yakimenko, Pair Spectrometer for FACET-II., *JACoW IPAC 2021*, 4336 (2021).